Numerical investigations of flow around subsea covers at high Reynolds numbers

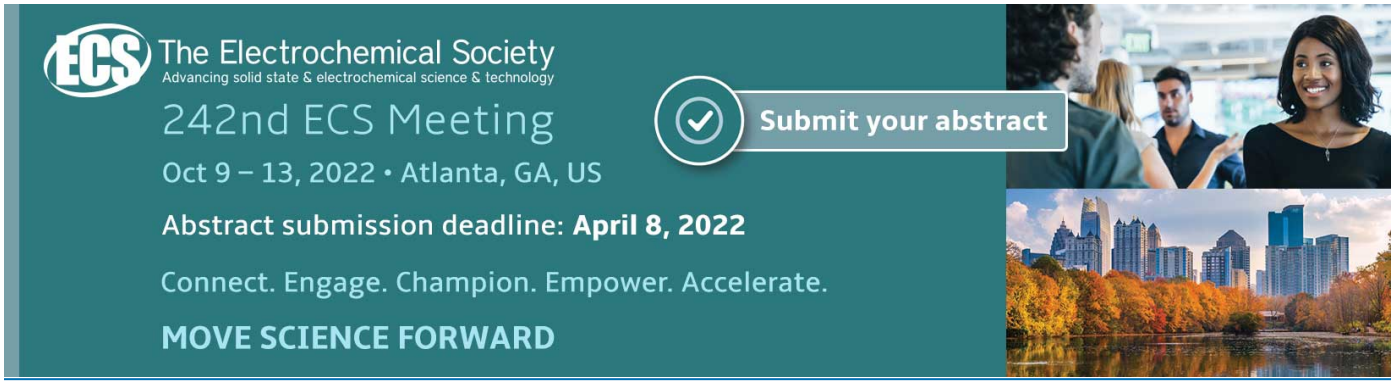

Numerical investigations of flow around subsea covers at high Reynolds numbers

G Yin*, Y Zhang and M C Ong

Faculty of Science and Technology, University of Stavanger, Norway

* Contact author: guang.yin@uis.no

Abstract. Two-dimensional (2D) numerical simulations of flow over wall-mounted rectangular and trapezoidal ribs subjected to a turbulent boundary layer flow with the normalized boundary layer thickness of $\delta/D = 0.73, 1.96, 2.52$ (D is the height of the ribs) have been carried out by using the Reynolds-averaged Navier-Stokes (RANS) equations combined with the $k-\omega$ SST (Shear Stress Transport) turbulence model. The angles of the two side slopes of trapezoidal rib varies from 0° to 60°. The Reynolds number based on the free-stream velocity U_∞ and D are 1×10^6 and 2×10^6. The results obtained from the present numerical simulations are in good agreement with the published experimental data. Furthermore, the effects of the angle of the two side slopes of the trapezoidal ribs, the Reynolds number and the boundary layer thickness on the hydrodynamic quantities are discussed.

1. Introduction

Investigations on turbulent flow over wall-mounted, sharp-edged ribs are of great importance due to their wide applications in industries such as gas turbines, heat exchangers and subsea covers for pipelines and other subsea equipment. For example, in subsea environments, these rib structures are commonly under high Reynolds number flow conditions. According to the measurements reported by Kuijpers & Nielsen (2016), the typical maximum current velocity near the seabed is in the order of $1\,\mathrm{m/s}$. Thus, the Reynolds number (defined as $Re = U_\infty D/\nu$) based on the characteristic height of the rib structures $D = 1\mathrm{m}$ is 1×10^6. Unlike the problems of flow around circular cylinders, the separation point of the flow is fixed at the leading corner of the rib structures and the presence of the wall can suppress the vortex shedding behind the rib structures. However, the shape of the rib structures still strongly influences the surrounding flow fields and the hydrodynamic forces on the structures. In the present study, the hydrodynamic quantities of the flow over wall-mounted rectangular and trapezoidal ribs are obtained by using 2D numerical simulations.

Several experimental and numerical studies have been performed to investigate the flow over wall-mounted structures at high Reynolds numbers. Arie et al. (1975) carried out experiments to investigate the pressure distribution around a wall-mounted square rib structure subjected to a turbulent boundary layer at Reynolds numbers ranges from 3.14×10^4 to 1.19×10^5 and it was found that the drag coefficient on the square decreases with the increasing boundary layer thickness. Wind tunnel experiments were conducted by Castro (1984) on flow over a wall-mounted 2D rectangular ribs with different aspect ratio between the width and height. It was found that the reattachment length of the separated shear layer behind the rib decreases linearly with the increasing rib width. Liu et al. (2008)

performed experimental study on the turbulent flow over a square rib at $Re = 1.32 \times 10^4$ with a normalized boundary layer thickness of $\delta/D = 0.75$. The unsteadiness of the wake flow was revealed.

Acharya et al. (1994) used RANS based on the nonlinear $k-\varepsilon$ turbulence model to carry out simulation on the flow over a 2D square rib in a turbulent channel. A good prediction of the turbulent kinetic energy and the velocity profiles were obtained. Tauqeer et al. (2017) has further studied the flows over ribs with different geometries subjected to a turbulent boundary layer with various δ/D. Different flow features over the square, triangular and semi-circular ribs were investigated. Yin et al. (2020) used 2D RANS simulations to study the boundary layer flow over two wall-mounted structures with square and trapezoidal shape in tandem on a horizontal flat wall and investigated the effects of the gap ratio between the two structures on the surrounding flow fields. Serta Fraga et al. (2020) and Yin & Ong (2020) performed 3D Spalart-Allmaras Delayed Detached-Eddy Simulations for flows over wall-mounted structures and the spatiotemporal characteristic of the wake flow behind the structures were studied using modal analysis. Andersen et al. (2021) investigated the boundary layer flow over a trapezoidal wall-mounted structures with different slope angles of the two sides. The influences of the slope angles on the hydrodynamic forces exerted on these structures were discussed.

In the present study, RANS model is used with the $k-\omega$ SST turbulence model. Two high Reynolds numbers (1×10^6 and 2×10^6) are considered. The boundary layer thicknesses δ/D under investigation are 0.73, 1.96 and 2.52. The length of the bottom edge of the ribs is kept the same so that the effects of the slope of the two sides of the trapezoidal ribs on the hydrodynamical quantities (such as the drag coefficients and the lift coefficients) can be elucidated. The paper is organized as follows: the governing equations and the computational overview are presented in Section 1; the convergence and validation studies are given in Section 2. Results and discussion are shown in Section 3; the conclusions are made in Section 4.

2. Numerical formulation

2.1. Flow model

The 2D steady RANS equations for conservation of mass and momentum are used in the present study and are given as

$$\frac{\partial \bar{u}_i}{\partial x_i} = 0 \tag{1}$$

$$\bar{u}_j \frac{\partial \bar{u}_i}{\partial x_j} = -\frac{1}{\rho}\frac{\partial P}{\partial x_i} + \frac{\partial}{\partial x_j}\left((\nu + \nu_T)(\frac{\partial \bar{u}_i}{\partial x_j} + \frac{\partial \bar{u}_j}{\partial x_i})\right) \tag{2}$$

where P is the mean pressure; ρ is the fluid density and ν is the fluid viscosity ($i, j = 1,2$. x_1 and x_2 denote the streamwise and cross-stream direction which are also denoted as x and y). The term ν_T denotes the eddy viscosity which is resolved by using $k-\omega$ SST turbulence model. The $k-\omega$ SST turbulence model is a combination of the standard $k-\omega$ model in the near-wall region and the standard $k-\varepsilon$ model in the outer wake region. A detailed description of the model can be found in Menter et al. (2003).

2.2 Computational domain and boundary conditions

The computational domain with a size of $60D \times 20D$ is employed for the present study as shown in Figure 1. The origin of the coordinates system is located at the center of the bottom edge of the rib structures. The inlet boundary is set to be $20D$ upstream from the center of the structure and the outlet is set to be $40D$ downstream from the center of the structure. These distances are determined based on the study reported by Ong et al. (2010), where the numerical study of flow around a circular cylinder close to a flat seabed was performed and the distances from the inlet and outlet boundary to the center of the cylinder are $10D$ and $20D$, respectively. Therefore, the computational domain is sufficiently large for the present study. The boundary conditions for the simulations are listed as follows:

i. The inlet flow is a boundary layer flow with a logarithmic velocity profile. The velocity profile is obtained by curve fitting of the experimental measurements reported by Arie et al. (1975) to guarantee the same experimental set-up for the validation of the results. The inlet value of k and ω are given by:

$$k(y) = \max\{C_\mu^{-0.5}(1 - y/\delta) \times |1 - y/\delta| u^{*2}, 0.0001U_\infty^2\} \quad (3)$$

$$\omega = k^{0.5}/(C_\mu^{0.5} l) \quad (4)$$

$$l = \min\{\kappa y(1 + 3.5\, y/\delta)^{-1}, C_\mu \delta\} \quad (5)$$

Here $C_\mu = 0.09$ and u^* is the friction velocity. κ is the von Karman with the value of 0.41. l is the turbulent length scale (Ong et al., 2010).

ii. No-slip condition is applied on the rib surface and the bottom wall with $u_1 = u_2 = 0$. Zero gradient is applied for the pressure. The standard wall function is employed for k and ω.

iii. At the outlet, u_1, u_2, k and ω are specified as zero gradient and the pressure is set be zero.

iv. At the top, u_1, u_2, k, ω and the pressure are set as zero gradient.

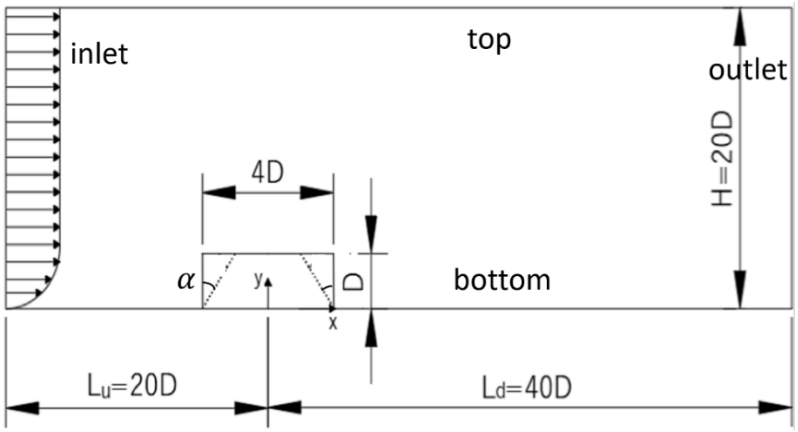

Figure 1. The computational domain.

2.3 Convergence studies

A grid convergence test is essential for any CFD simulation to check whether the results obtained are independent on the grid resolutions. The drag coefficient C_d as well as the lift coefficient C_l at high Reynolds number flows are of primary interest for the further study. The value of C_d is defined as $C_d = 2F_D/(\rho U_\infty^2 A_x)$ and the value of C_l is defined as $C_l = 2F_L/(\rho U_\infty^2 A_y)$, where F_D and F_L are the drag and lift forces acting on the structure in the streamwise and cross-stream directions and A_x and A_y are the projected areas in the two directions. The results of simulations at the highest investigated Reynolds numbers at $Re = 2.0 \times 10^6$ with $\delta/D = 0.73$ are shown in Figure 2. The relative difference of C_d and C_l between cases obtained in present study all falls within the convergence criteria of less than 5%. Thus, it can be concluded that sufficient grid resolution has been achieved among all cases in present study. Since the wall functions are applied for all the simulations, the log-law layer has a region of $y^+ > 30$. In the present study, y^+ varies between 30 and 42 for the square and trapezoidal structures in all cases.

2.4 Validation study

The validation is performed by comparing the present predicted horizontal velocity profiles around a wall-mounted square structure with experimental data reported by Liu et al. (2008) as shown in Figure 3.

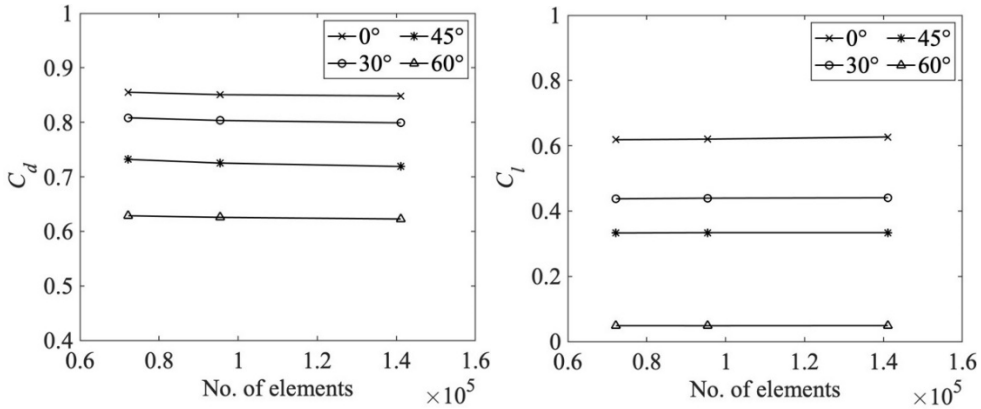

Figure 2. Mesh Convergence with respect to hydrodynamic coefficients C_d (left) and C_l (right) at $Re = 2.0 \times 10^6$ with $\delta/D = 0.73$.

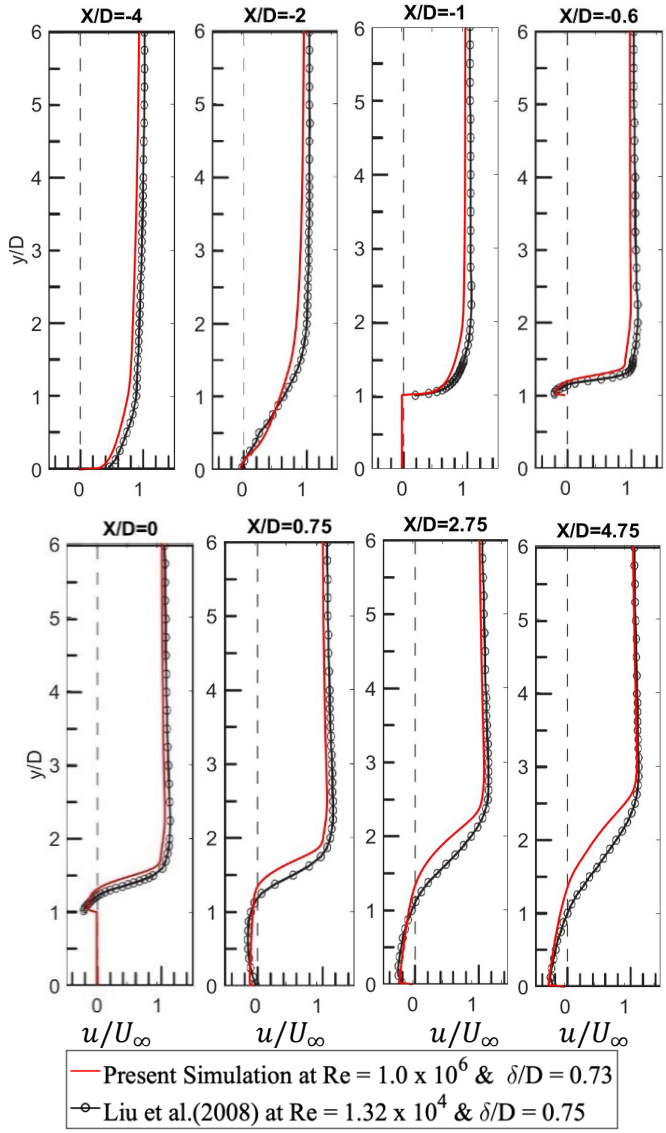

Figure 3. Comparisons of the horizontal velocity profiles of the present simulation and the experimental data from Liu et al. (2008).

The horizontal velocity profiles are selected at eight different locations along the x-axis in the computational domain. Two of them are the velocity profiles at the upstream of the structure, located at $x/D = -4$ and $x/D = -2$, respectively. Three of them are on the square structure and the other three are located in the downstream of the structure. It can be observed that the numerical results are generally consistent with the experimental data, especially in the upstream of the structure and on the structure. However, a gradually increasing deviation from the experimental profile occurs in the downstream of the structure from the location of $x/D = 0.75$. The negative parts in the velocity profiles indicating a recirculation zone behind the square structure is captured in the wake region close to the bottom.

3. Results and discussion

3.1 Effects of the slope angle α on hydrodynamic coefficients

The effect of the slope angle α on the hydrodynamic quantities has been studied at $Re = 1.0 \times 10^6$ and $Re = 2.0 \times 10^6$ with the boundary layer thickness of $\delta/D = 0.73\sim2.52$. The variations of C_d and C_l with respect to the slope angle of $\alpha = 0°, 30°, 45°, 60°$ are shown in Figure 4. At both Reynolds numbers, the lift and the drag coefficients are monotonically declining as the slope angle rises. For the values of the drag coefficient C_d, with the increasing the slope angle, the block effect of the structure to the flow becomes weaker. The pressure difference between the front face and back face decreases, which leads to a decreasing C_d. For the value of C_l, it should be mentioned that the projected areas (the bottom areas of the structures) for all structures are the same as shown in Figure 1. Therefore, the decreasing C_l is due to the decreasing lift force. The reason for the decreasing lift force can be explained as follows: with the increasing α, the flow velocity above the structure drops, resulting in a reducing negative pressure above the structure, which leads to the decreasing lift force.

(a)

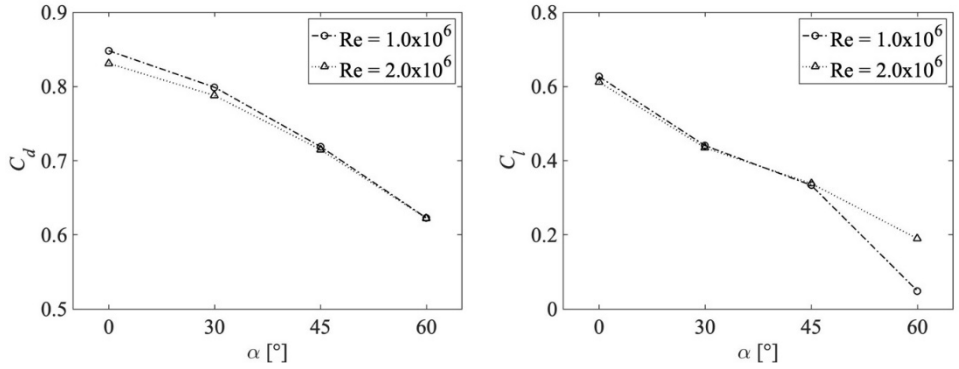

(b)

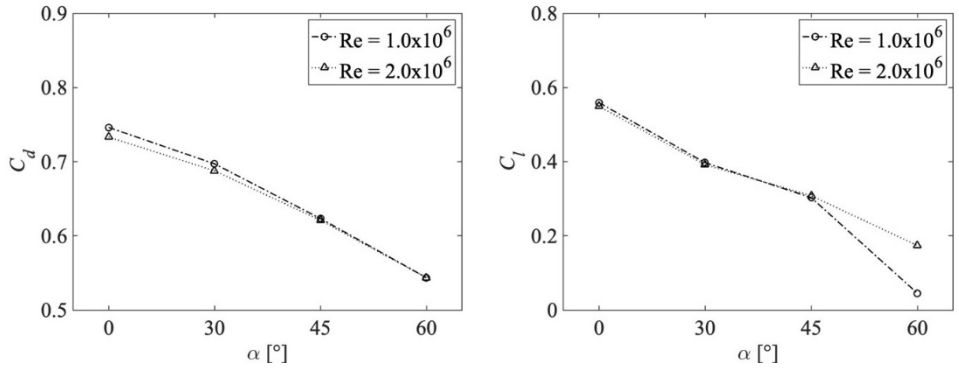

(c)

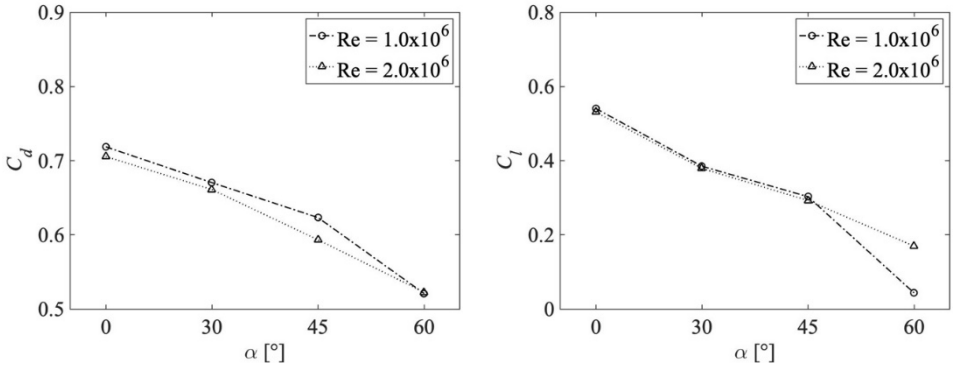

Figure 4. Variation of hydrodynamic coefficients with α for different boundary layer thicknesses: (a) $\delta/D = 0.73$, (b) $\delta/D = 1.96$ and (c) $\delta/D = 2.52$.

3.2 Effects of Reynolds number on hydrodynamic coefficients

A further study on the effect of Reynolds numbers on hydrodynamic quantities C_d, C_l has been carried out for the structures with all α at $Re = 1.0 \times 10^6$ to $Re = 2.0 \times 10^6$. From Figure 5, it can be seen that in general, the value of C_d increases as Reynolds number increases. However, with $\alpha = 60°$, the variation of C_d with the Reynolds number is barely visible. This can be attributed to the reason that with $\alpha = 60°$, the structure tends to be flat, and the two slopes are close to be horizontal. The resulting contribution of pressure difference to the drag decreases while the contribution of the viscous force increases. At the investigated high Reynolds number, the viscous effect is small. Therefore, the small variation of C_d with the Reynolds number is observed.

Apart from the increasing C_d with the increasing Reynolds number, it is also found that the lift coefficient C_l slightly increases with the increasing Reynolds number as the slope angle α varies from 0° to 30°. Nevertheless, an adverse effect on C_l is observed as Reynolds number increases for the case with $\alpha = 60°$.

(a)

(b)

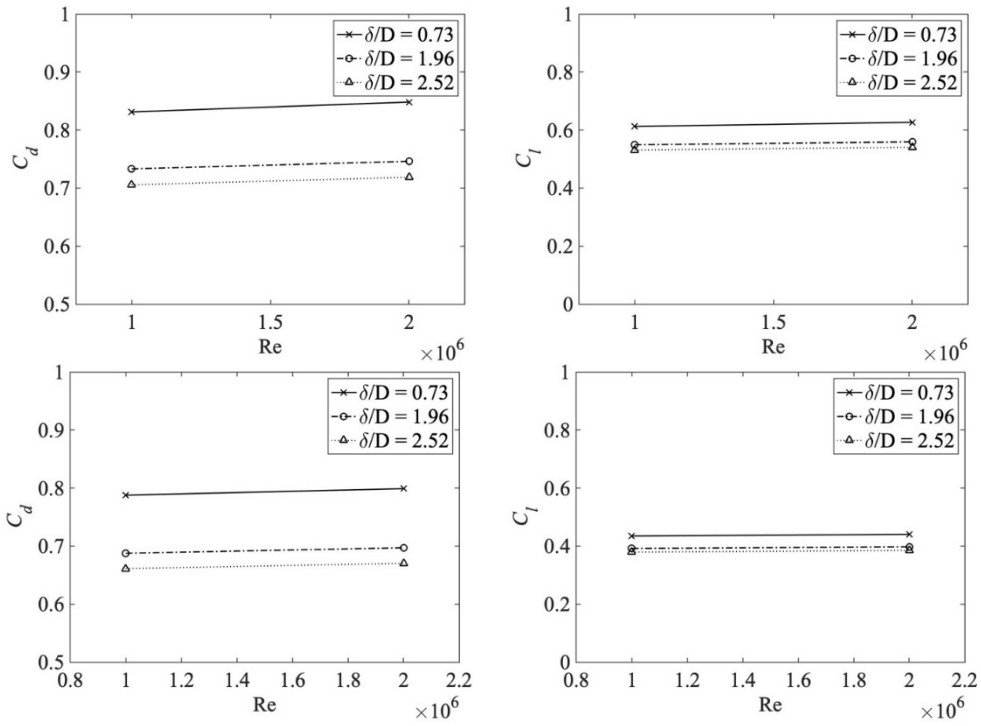

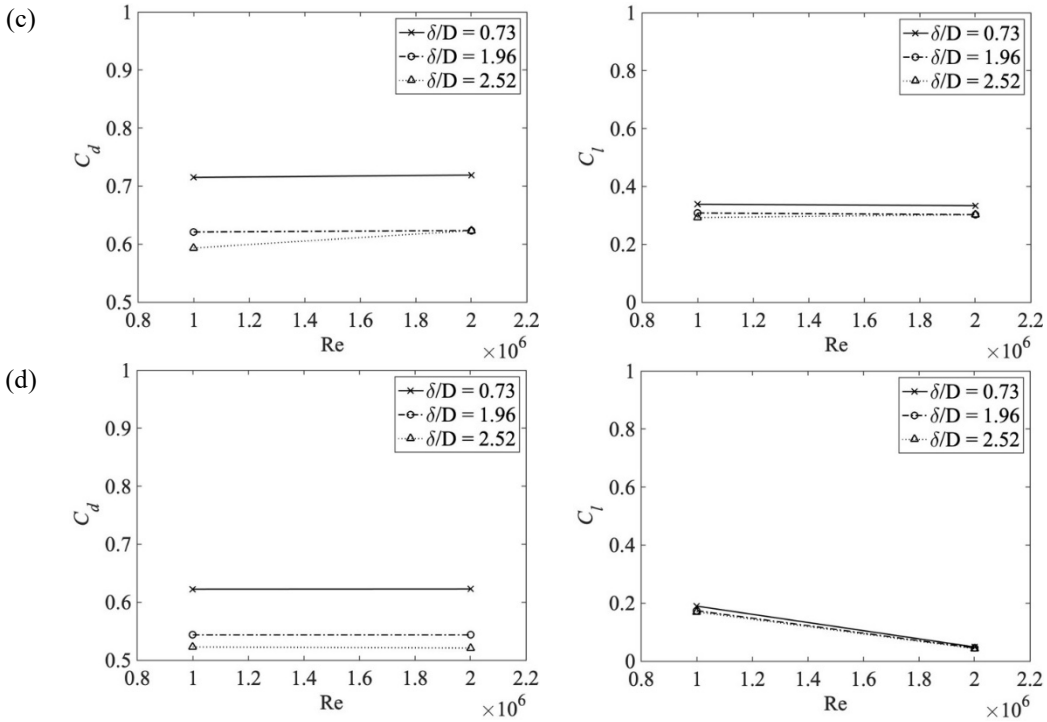

Figure 5. Variation of hydrodynamic coefficients with Reynolds numbers for different angles of slope: (a) $\alpha = 0^{\circ}$, (b) $\alpha = 30^{\circ}$and (c) $\alpha = 45^{\circ}$, (d) $\alpha = 60^{\circ}$.

3.3 Effects of δ/D on hydrodynamic coefficients

The effect of normalized thickness δ/D on the hydrodynamic quantities is investigated with $\delta/D = 0.73, 1.96$ and 2.52, as shown in Figure 6. It can be seen that both C_d and C_l decreases as δ/D increases. This is due to the fact that the increase in δ/D causes a drop in averaged velocity of the boundary layer flow that the structure is subjected to. Consequently, the pressure around the structure decreases, resulting in a decreasing force on the structure.

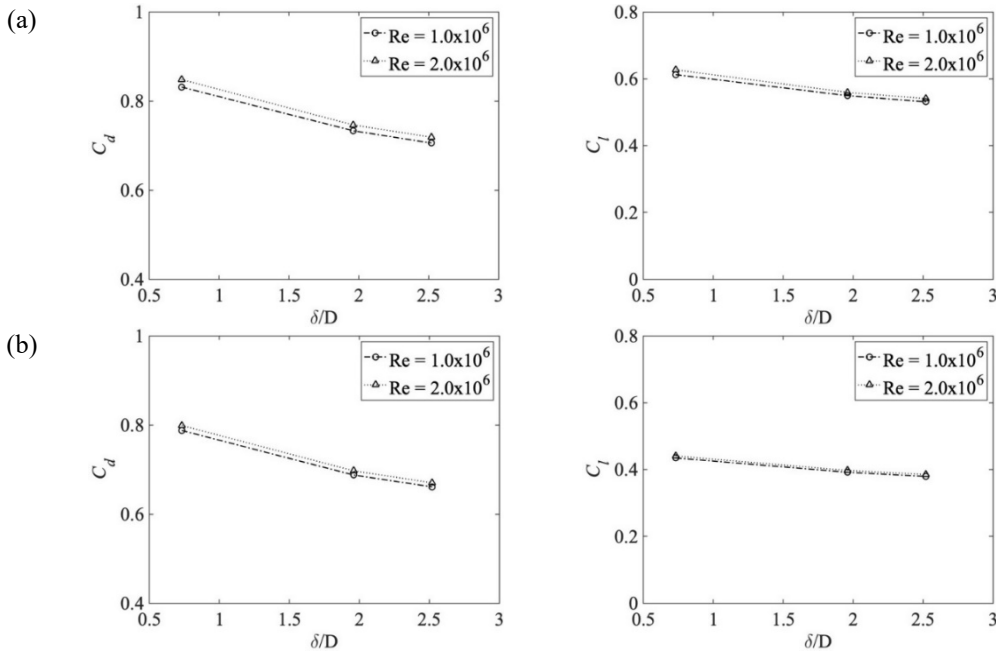

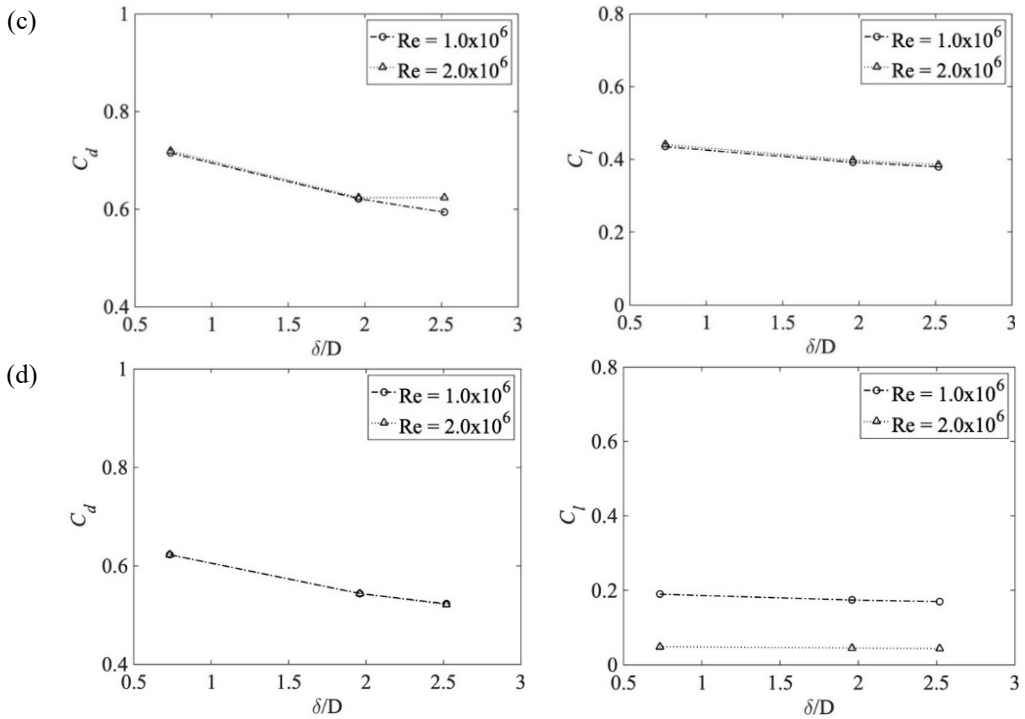

Figure 6. Variation of hydrodynamic coefficients with respect to different boundary layer thicknesses at different angles of slope: (a) $\alpha = 0^{\circ}$, (b) $\alpha = 30^{\circ}$and (c) $\alpha = 45^{\circ}$, (d) $\alpha = 60^{\circ}$.

3.4 Pressure distribution

The drag and lift forces are mainly determined by the pressure difference around the structure. Therefore, it is necessary to investigate the pressure distributions in the flow field. The pressure distributions around the rectangular and trapezoidal structures are presented in this section. The contours of the pressure distributions for $\alpha = 0°, 30°, 45°, 60°$ at $Re = 1.0 \times 10^6$ with two δ/Ds are presented in Figure 7. A high-pressure region is observed in front of the structure due to the block effect of the structure on the incoming flow. Additionally, two low-pressure regions can be observed for $\alpha = 0°$ in Figure 7. The first one is located above the rectangular structure after the separation point at the leading corner due to the flow separation. The other one is formed behind the structure due to the recirculation behind the structure. Moreover, according to the mass conservation law, an increase in the velocity is caused due to the flow separation. Hence, the increase in the velocity leads to a decrease in the pressure according to the Bernoulli's equation. With the increasing δ/D, the velocity change of flow decreases, and the amplitude of the pressure decreases.

It can be observed that due to the weakened block effect with the increasing α, the pressure amplitude decreases, which is in consistence with the variation of C_d and C_l in Section 3.1. It is also worth noting that from $\alpha = 45°$ to $\alpha = 60°$, with the increasing δ/D, the center of the low-pressure region behind the structure is detached from the back face of the structure and moves further downstream.

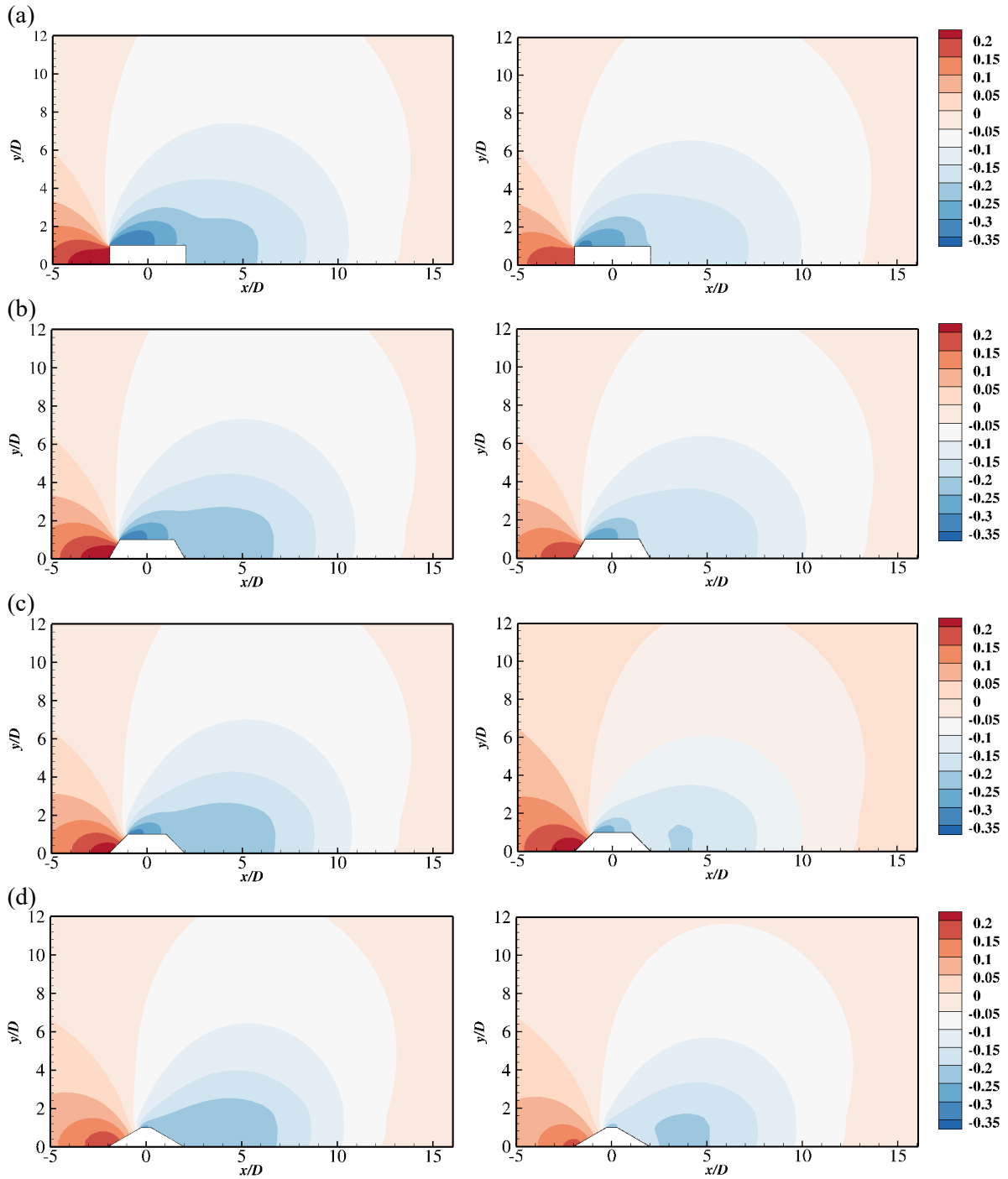

Figure 7. The pressure fields for the wall-mounted structures with (a) $\alpha = 0°$; (b) $\alpha = 30°$; (c) $\alpha = 45°$; (d) $\alpha = 60°$ at $\mathrm{Re} = 1 \times 10^6$ and right (left) $\delta/D = 0.73$ and (right) $\delta/D = 2.52$.

4. Conclusion

Numerical investigations of the turbulent boundary layer on surface-mounted subsea covers of different geometries have been performed. Two-dimensional steady RANS equations are solved by $k-\omega$ SST turbulence model combining with the wall function. A mesh convergence study has been conducted to ensure that the numerical results are independent on the grid resolutions. The relative difference of drag coefficient C_d and lift coefficient C_l between the course, medium and fine meshes are within a

reasonable range. The convergence study has proved that the meshes used in the present study have achieved sufficient grid resolutions. Furthermore, the validation study is conducted by comparing the horizontal velocity profiles around a wall-mounted square structure obtained in the present study with the experimental data published by Liu et al (2008). The validation study shows a good agreement between the present simulation results and the experimental data. This indicates that the present RANS simulations with the $k-\omega$ SST model can give a satisfactory prediction the flows over a wall-mounted structure subjected to a boundary layer flow at high Reynolds numbers.

Results from the simulations have been further discussed. Based on the analysis of the effects of the slope angles of the two sides of the structures, Reynolds numbers and the boundary layer thicknesses on the hydrodynamic coefficients of the structures, the following conclusions can be drawn:

1. For the trapezoidal structures, the hydrodynamic quantities including both C_d and C_l decrease monotonically as α increases.
2. For trapezoidal structures with the angle ranging from 0° to 45°, the value of C_d increases as the Reynolds number increases. The pressure drag force provides a major contribution to drag force at high Reynolds numbers. However, the frictional drag due to the viscous effect still accounts for the total drag force for the geometry with $\alpha = 60°$.
3. The hydrodynamic quantities decrease as the boundary layer thickness increases due to the drop in the averaged velocity of flow the structures are subjected to.

References

[1] Acharya S, Dutta S, Myrum T A and Baker R S 1994 Turbulent flow past a urface-Mounted Two-Dimensional Rib. ASME. *J. Fluids Eng*. **116**(2), 238–246.
[2] Andersen M, Yin G. and Ong M C 2021 Numerical Simulations of Flow Around Wall-Mounted Square and Trapezoidal Structures at High Reynolds Numbers. *J. Offshore Mech. Arct. Eng.* **143**(1), p.011902.
[3] Arie M, Kiya M, Tamura H, Kosugi M And Takaoka K 1975 Flow over rectangular cylinders immersed in a turbulent boundary layer: Part 2 flow patterns and pressure distributions. *Bulletin JSME*. **18**(125), 1269-1276.
[4] Kuijpers A and Nielsen T 2016 Near-bottom current speed maxima in North Atlantic contourite environments inferred from current-induced bedforms and other seabed evidence. *Mar. Geol.* **378**, 230-236.
[5] Liu Y Z, Ke F and Sung H J 2008 Unsteady separated and reattaching turbulent flow over a two-dimensional square rib. *J. Fluids Struct.* **24**(3), 366-381.
[6] Menter F R, Kuntz M and Langtry R 2003 Ten years of industrial experience with the SST turbulence model. *Turbul. Heat Mass Transfer*. **4**(1), 625-632.
[7] Ong M C, Utnes T, Holmedal L E, Myrhaug D and Pettersen B 2010 Numerical simulation of flow around a circular cylinder close to a flat seabed at high Reynolds numbers using a k–ε model. *Coastal Eng.* **57**(10), 931-947.
[8] Serta Fraga V, Yin G and Ong M C 2021 Three-dimensional numerical simulations and proper orthogonal decomposition analysis of flow over different bottom-mounted ribs. *Ships Offshore Struct.* 1-36.
[9] Tauqeer M A, Li Z and Ong M C 2017 Numerical simulation of flow around different wall-mounted structures. *Ships Offshore Struct.* **12**(8), 1109-1116.
[10] Yin G, Andersen M and Ong M C 2020 Numerical simulations of flow around two tandem wall-mounted structures at high Reynolds numbers. *Appl. Ocean Res.* **99**, 102124.
[11] Yin G and Ong M C 2021 Numerical analysis on flow around a wall-mounted square structure using Dynamic Mode Decomposition. *Ocean Eng.* **223**, 108647.